Investigation into Camera Calibration Flight Paths for UAV-Based Corridor Surveys

Jack Henharen, Petra Helmholz

School of Earth and Planetary Sciences, Spatial Sciences, Curtin University
GPO Box U1987, Perth WA 6845, Australia –henharen.jack@gmail.com; Petra.Helmholz@curtin.edu.au

Commission II/WG 1

KEYWORDS: Camera calibration, digital elevation models, systematic errors, structure from motion, radial distortion correction.

ABSTRACT:
There is increasing adoption of cost-effective nonmetric camera-equipped unmanned aerial vehicles due to the perceived benefits of timesaving, ease of use, and the accuracy of the digital elevation models that can be produced using structure from motion software. The introduction of systematic elevation errors, doming and bowing, has been evidenced by several authors, and various methods have been identified to reduce these errors. This paper aims to analyse the impact of flight plans on these systematic errors using the especially challenging case of a corridor survey. Two sites were flown for the survey using a DJI Zenmuse. The first site, a car park, was utilised for on-the-job pre-calibration of the camera and consisted of several orbit flights and a double grip flight. Subsequently, an adjacent road (a corridor survey overall 428 m long) was also surveyed at 60 m and 80 m heights using varying flight configurations. This study confirms that pre-calibrating the camera's IOPs significantly reduces the root mean squared elevation error (from 0.268 m to 0.034 m) compared to self-calibrated IOPs using the corridor flights. The impact of flight design on elevation errors confirms a single flight path's risk and the benefits of two or more flight paths, including a point-of-interest orbit flight.

1. INTRODUCTION

The introduction of cost-effective nonmetric camera-equipped unmanned aerial vehicles (UAV), along with the development of structure from motion (SfM) software, has recently become a convenient platform for surveyors to capture a range of diverse data upon the surface of the earth and aid in creating intricate georeferenced 3D digital elevation models (DEM) (Eltner & Schneider, 2015; Ouédraogo et al., 2014; Turner et al., 2012). There has been rapid adoption of these UAV systems in a variety of sectors, ranging from open-pit mining to pipeline and rail corridor inspections (Bojarczak & Lesiak, 2021; Park & Choi, 2020), given an often-emphasised potential for timesaving, ease of use and the DEM quality that can be achieved.

The accuracy of the DEM produced depends on several variables, including site topography, camera sensor quality and SfM processing software. Therefore, relative model accuracy and precision improvements are to be gained in controlling the variables of ground control point (GCP) referencing, flight design, and the often-overlooked camera calibration. Accurate camera calibration is crucial for DEM creation. Systematic errors are commonly found in the SfM-derived DEM when using inaccurate camera calibrations in the absence of a metric camera sensor. The most typical errors are systematic 'doming' and 'bowing'. (Griffiths and Burningham, 2018; Sanz-Ablanedo et al., 2020; Yurtseven, 2019).

These systematic errors affect the DEM, causing it to homogeneously concave upwards or downwards. Due to the geometry of aerial data capture, systematic errors are generally only realised on the vertical axis (Sanz-Ablanedo et al., 2020). Incorrect radial distortion camera parameters have been identified as the cause of these doming and bowing errors (James et al., 2017; James and Robson, 2014; Sanz-Ablanedo et al., 2020). It has been demonstrated (Fraser, 1997; James and Robson, 2014; James et al., 2019) that the error associated with the systematic distortion can be reduced to a point where the quality of GCP georeferencing dictates the DEM's overall accuracy through the optimisation of an accurate camera self-calibration.

In part, the increasing costs of traditional-based survey works have led to increased demand to provide lower-cost DEMs with ever-increasing accuracy identifying and mitigating these errors is essential. Error detection can be performed relatively easily using checkpoints (CP); however, increasing the number of GCPs and CPs is not always commercially viable or practical. Commercial pressures favour adopting flight designs for extensive corridor surveys to reduce the time spent on site versus implementing best practice flight patterns to achieve accurate camera self-calibration models using in-mission imagery. Whilst these techniques improve accuracy, the survey camera's calibration aspect appears to be overlooked. Sets of images with poor convergent imagery and parallel viewing directions have been found to incorrectly calculate radial distortion correction and the interior orientation parameters (IOP) of self-calibrated cameras (James et al., 2019).

While previous studies focused on different calibration models (Cledat at el., 2020) or the variation of the location and number of control points (Villanueva and Blanco, 2019), this study investigated the optimisation of in-mission camera self-calibrations in varying flight patterns for a road corridor survey. To achieve this, the impact of the flight path configurations on the IOP and the relationship between radial distortion corrections were analysed. In addition, the impact of on-the-job pre-calibration on flight configuration accuracy is assessed.

This paper is structured as follows: After presenting the study area in section 2, the method is introduced in section 3, followed by the results in section 4. The paper is concluded including a discussion of the results in section 5.

2. STUDY AREA

2.1 Location

The Bentley campus of Curtin University in Western Australia provided a local site with limited public traffic during the study duration. Karrak Drive and the PA2 car park, situated west of the campus, provide a corridor length of just over 400m, with minimal changes in grade. This allowed uninterrupted data collection on private land without interfering with the public. Figure 1 presents the whole area with car park PA2 located on the left side of the figure (yellow circle) and Karrak Drive (red ellipse). Figure 2 shows a detailed view of PA2 rotated 90 degrees counterclockwise compared to Figure 1.

Figure 1: UAV image capture areas within Curtin University Bentley campus: (1) PA2 Carpark (yellow), (2) Karrak Drive (red).

Figure 2: Detailed layout of GCP in PA2 Carpark.

2.2 Ground Control

To simulate standard operating procedures for survey fieldwork, a total of five GCPs were situated using real-time kinematic (RTK) GNSS (Trimble R12) along Karrak Drive. Two independent sets of five-minute RTK observations were made utilising two test network GNSS pillars (Landgate, 2019) for base stations 500 m and 740 m from the test site. GCPs were located at the north (GCP 9) and northeast end (GCP 14), at the southern end (GCP 28), the southwest end (GCP 29) and GCP33 was located at the 200 m chainage. Using the same GNSS method, 13 CPs were installed along the alignment at approximately 20 m intervals (Figure 1).

The distance between GCPs was deliberately increased to 200m, along chainage, to accentuate the impact of doming or bowing on the model. The CPs were included to quantify errors. To generate the pre-survey camera calibration, an additional 15 GCPs were situated at even spacings within the PA2 car park study area.

2.3 Field Data Collection and Flight Configurations

The UAV used was a commercial grade UAV (DJI Matrice 200) fitted with a DJI Zenmuse X4S FC6510 20MP 1" sensor mounted to the 180-degree gimbal, with a stated 8.8 mm focal length and an effective 20 megapixels giving a pixel size of 3µm. The UAV's RTK system was disabled to simulate a consumer-grade drone. Camera settings such as focal length were kept constant for all flights.

Aerial survey planning was completed using DroneDeploy (DroneDeploy, 2023), with nine flight paths completed over the two flight areas. Three flights were conducted over the PA2 car park, and six were conducted over Karrak Drive.

The three flights over the PA2 car park consisted of two grids flown at a height of 60 m and 80 m and an orbit around the central point at a height of 80 m covering a 140 m x 100 m (14,000 m^2) area (**Error! Reference source not found.**).

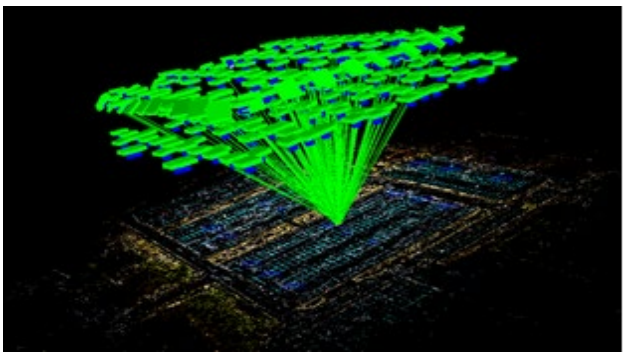

Figure 3: iWitnessPro 3D View; camera locations above the PA2 Carpark.

The six flights over Karrak Drive were done in three configurations (Table 1), each using two different flight heights. Given the UAV's stated sensor size and flying heights of 60 m and 80 m, a respective ground scale distance of 1.73 cm/pixel and 2.26 cm/pixel in the nadir direction was achieved.

The flight configurations include a parallel flight (back and forth along the corridor with a 60-degree oblique viewing angle, achieving a forward image overlap of 90% and 70% lateral overlap), a grid flight including areas next to the corridor, and a point-of-interest (POI) flight where the camera points constantly towards the centre of the survey area.

Flight Path	Image Height	# Images
Oblique Corridor	60m	34
	80m	25
Grid	60m	64
	80m	36
Point-of-Interest Corridor	60m	40
	80m	31

Table 1. Flight paths flown over Karrak Drive.

Several image sets were processed by combining those flights, as shown in Table 2. Figure 4 visualises the camera locations for image set 8 combining a 60 m oblique corridor flight with a 60m POI flight. The figure highlights the rays of a central point captured by images of the POI flight.

Image Set	60 m Corridor	80 m Corridor	60 m Grid	80 m Grid	60 m POI Orbit	80 m POI Orbit
1	Y	-	-	-	-	-
3	Y	Y	-	-	Y	-
4	Y	-	-	Y	-	-
5	-	Y	Y	-	-	-
6	Y	-	-	-	-	Y
7	-	Y	-	-	Y	-
8	Y	-	-	-	Y	-
9	Y	-	Y	-	-	-
10	-	-	Y	-	-	-

Table 2. Karrak Drive flight paths utilised in processed image sets.

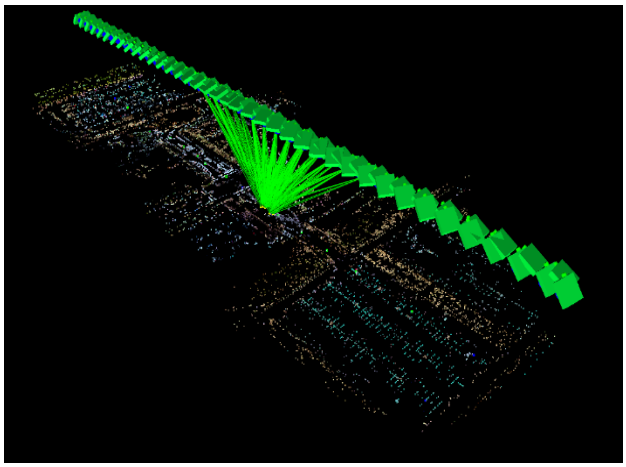

Figure 4: iWitnessPro 3D View; set 8 image locations above Karrak Drive.

3. METHODS

3.1 Camera Calibration Processing

iWitnessPro V4.105 was used to complete camera calibrations, image matching, and point cloud model creation. A targetless orientation procedure was performed to relatively orientate the images and aid in the GCP image observations. An estimated focal length for the camera system is calculated during the process. During the targetless orientation process, the option for 'Image GPS data for pair selection and bundle adjustment aid' was preemptively disallowed. This increased the computation times. However, it ensured that the software would disregard no image matches. Preliminary modelling of camera radial distortion parameters was allowed, and the maximum number of feature-based points was set to 40,000. As advised by the software developers, since manual GCP selection was to be completed, the point cloud was thinned, decreasing processing time significantly without impacting future bundle adjustment accuracy (Photometrix, 2018). The software suggests reducing the tie points and, therefore, redundancy due to the addition of GCPs.

A controlled bundle adjustment is completed to calculate the camera's IOPs, with all camera IOPs to be estimated. All image observations are equally weighted with 1 pixel. This adjustment calculates ten IOPs, consisting of the focal length (*c*), principal point offsets for the x-axis (*PP x*) and y-axis (*PP y*), radial distortion correction terms of the 3rd (*K1*), 5th (*K2*) and 7th (*K3*) order, coefficient of decentering distortion *P1* and *P2*, differential scaling between x and y axis (*B1*) with non-orthogonality between x and y axis (*B2*).

Outputs for further analysis were the camera's IOPs, radial distortion corrections, estimated self-calibration quality, and the object space coordinates for CPs. Finally, a dense automated point cloud was generated, producing a .las file for point cloud analysis for each project.

3.2 Configurations

3.2.1 On-the-job pre-calibration using PA2 test site. The on-the-job calibration of the camera was processed using all 239 images captured of the PA2 car park (Figure 3). While it is known that a car park is generally not the most desirable place for calibration due to missing variations of heights and well-defined features in object space, the car park was used due to the lack of alternatives. To still achieve a reliable calibration, six GCPs within the PA2 car park (GCP 8, 10, 11, 12, 14 and T4) were introduced. The GCPs were arranged in an evenly spaced grid pattern around the PA2 car park (Figure 2; Figure 3). These GCPs were observed in as many images as possible with high accuracy.

For simplification purposes, we refer to this calibration as "Pre-calibration (Pre-Cal)" instead of on-the-job calibration. On-the-job calibration is more appropriate, as, in principle, a self-calibration of the camera was still performed. However, as we fixed the camera's IOPs for all the following jobs, this could be seen as a pre-calibration.

3.2.2 Self-calibration along Karrak Drive. The different image sets processed were introduced in Table 2. Each image set was processed in two independent projects, defined by S_Cal (self-calibrated), and Pre-Cal (pre-calibrated). The Pre-Cal projects used the pre-calibrated camera IOPs calculated using the PA2 car park flights. In contrast, a self-calibration is performed for the S_Cal using the same default initial values (focal length set to 8.8 mm and all other IOPs set to 0). Otherwise, the pre-calibrated (Pre-Cal) and self-calibrated (S_Cal) projects were processed the same way. After targetless orientation, the same five GCPs (9, 14, 28, 29 and 33) (Figure 1) along Karrak Drive were used for both projects. Additionally, the 13 CPs placed along the corridor were observed. The same GCPs and CPs have been used for all configurations.

3.3 Analysis

3.3.1 General adjustment outputs. iWitnessPro V4 provides a measure called "Quality of Self-calibration", calculated during the bundle adjustment procedure. The only information provided in the software manual about this measure is "The Quality of Self Calibration has an optimal value of 1.0, values of 1.5 are considered acceptable. Values higher than 1.5 indicate a weak network geometry and thus sub-optimal determination of camera parameters." (iWitness, 2019).

Next, the root mean square of the image point residuals (*RMS Vxy*) was used as an indicator for the quality of the bundle adjustment. A value of less than 1 pixel is acceptable, considering the quality of the images, their overlap, and the high redundancy of the Least Square Adjustment.

The most common independent method to assess adjustment results is using CPs and their residuals. From each of the image sets (S_Cal and Pre-Cal), the calculated image space coordinates for the 13 CPs were exported for analysis. Four statistics were

used for the analysis: the maximum vertical error of CPs (Dome/Bowl Magnitude) – as an indicator of the magnitude of the bowing, the vertical RMS of CPs – to quantify the average vertical error found within the model, and the standard deviation of CPs.

The CP analysis will help quantify the magnitude of the bowing effect. A point comparison is also performed to provide a more complete overview and not be limited to the 14 CPs. The pre-calibrated set point clouds and their partner self-calibrated set point clouds were overlayed, and the point cloud models were trimmed to isolate the extended Karrak Drive corridor.

Then, a cloud distance computation was run on the z-axis to establish a scalar field comparison model. For the comparison, a point-to-model approach was used, meaning that a plane was fit through one point cloud using points in the k-nearest neighborhood (6knn) followed by calculating the distance along the normal vector to a point in the partner point cloud. For the point cloud analysis, CloudCompare V2.12.4 was utilised (*CloudCompare* 2022).

3.3.2 Camera Calibration Outputs (Analysis of IOPs). The analysis of camera calibration focused primarily on the radial distortion corrections, as previous studies have shown that there is a strong correlation between the bowing effect and radial lens distortion (Fraser, 1997; James and Robson, 2014; James et al., 2019). Hence, radial lens distortion profiles were plotted based on the car-park self-calibration (assumed to be the reference) and all self-calibration related to the road survey.

4. RESULTS

4.1 General Adjustment Outputs

The pre-calibration adjustment using the PA2 test site was successful. With the inclusion of exhaustive matching and error propagation modelling, the targetless orientation was completed in approximately 75 minutes and provided over 500,000 feature-based matches (FBM). The quality of the self-calibration had a value of 1.0, indicating a solid network geometry. The image referencing error is 0.49 pixels indicating that the images have been related relative to each other successfully. The GCP residuals were 0.006m and CP residuals 0.017m. Hence, a successful self-calibration of the PA2 test site was achieved, and as such, this camera calibration was considered successful.

Regarding the corridor survey, for all image sets, except for set 1, the calculated self-calibration accuracy calculated by iWitnessPro was a value of 1.0, and image set 1 was estimated at 1.1. Based on this information, all adjustments had a very good geometry. The average precision of image referencing is 0.47 pixels, with a standard deviation of 0.02 pixels. iWitnessPro also calculated the estimated 3D GCP RMS accuracy for all image sets at 0.024 m, with a standard deviation of 0.005 m. Based on these values, all adjustments were considered successful.

Table 3 shows the results of the self and pre-calibrated sets and quantifies the magnitude of the doming/bowing effect. The maximum height of the bowing was calculated based on the largest CP residual. The reduction of RMS (last column) shows how much the RMS was reduced when using the pre-calibrated IOPs, assuming that the self-calibration RMS is 100%. All maximal residuals of a CP with a value larger than 10 cm are highlighted in bold. Analysis of the self-calibrated sets provides indicative feedback on using self-calibration for corridor surveys.

All the self-calibrated image sets exhibited varying degrees of doming. The use of single flight images obtained through either a corridor (set 1) or grid (Set 10) flight path produced significant bowing of +0.645 m and +0.819 m, respectively and would not be considered suitable for survey purposes. The data indicates that including a second flight path reduces the doming significantly, with set 5 producing the lowest error of all the self-calibrated image sets at 0.082 m. This image set was generated from an 80 m corridor flight and a 60 m grid flight with no point of interest (POI) flight. The best POI and corridor combination came from set 8, utilising 60 m POI and 60 m corridor images to return a maximum doming of 0.117 m.

An analysis of the vertical RMS of self-calibrated image sets (Table 3) provided some interesting results. All RMS larger than 3 cm are highlighted in bold. When comparing corridor and grid image combinations, image set 4 comprised a lower corridor flight (60 m) and a higher grid flight (80 m), providing a GCP height RMS of 0.404 m. Image set 9 was generated from the corridor and grid flights at the same height of 60 m, and this combination returned an RMS of 0.338 m. In comparison, set 5 utilised a lower grid flight (60 m) and a higher corridor flight (80 m), significantly reducing the RMS to 0.051 m.

When observing the corridor and POI orbit combinations, image set 6 utilised the lower corridor flight (60 m) and a higher POI orbit (80 m) with a resultant RMS of 0.171 m, a significant improvement in RMS when compared to the corresponding corridor and grid flights at the same heights (set 4). Increasing the corridor height to 80 m while keeping the 60 m POI orbit (set 7) reduced the RMS to 0.102 m, providing an improvement in RMS compared to the similar corridor grid flight. Set 8 used the lower POI orbit images of 60 m while utilising the same 60 m corridor images as set 6, and this returned the best self-calibrated result using a corridor and POI flight, achieving an RMS of 0.087m.

Image Set	# Images	Self-Calibrated (S_Cal)				Pre-Calibrated (Pre-Cal)			Reduction RMS; Pre Cal - Self Cal
		Dome/Bowl Magnitude (m)	RMS (m)	Std.Dev (m)	Est. Quality of Self-Cal	Dome/Bowl Magnitude (m)	RMS (m)	Std.Dev (m)	
1	34	**0.645**	**0.502**	0.210	1.1	**0.238**	**0.117**	0.107	77%
3	100	**0.193**	**0.152**	0.064	1.0	0.027	0.015	0.014	90%
4	70	**0.512**	**0.404**	0.175	1.0	0.038	0.019	0.015	95%
5	89	0.082	**0.051**	0.027	1.0	0.038	0.018	0.011	65%
6	64	**0.243**	**0.171**	0.080	1.0	**0.091**	**0.056**	0.033	67%
7	65	**0.148**	**0.102**	0.051	1.0	0.035	0.023	0.014	78%
8	73	**0.117**	**0.087**	0.037	1.0	0.041	0.025	0.016	71%
9	98	**0.454**	**0.338**	0.154	1.0	0.009	0.006	0.005	98%
10	68	**0.819**	**0.606**	0.283	1.0	0.052	0.027	0.017	96%

Table 3. CP Vertical Error for Self-Calibrated and Pre-Calibrated Image Sets. All maximal residuals of a CP with a value larger than 10 cm are highlighted in bold.

The benefit of pre-calibration in reducing the effect of doming and bowing is clear (Table 3). It should be noted that the impact of pre-calibration on these flight images was to introduce a small amount of bowing in 78% of the sets. The most significant correction of systematic error can be seen in Set 9; Figure 5 illustrates this correction. The spectral grading of Figure 6 illustrates that the doming of 0.454 m at an RMS of 0.338 m for the self-calibrated model is reduced to a bowing of -0.009 m at an RMS of 0.006 m for the pre-calibrated model. Pre-calibration provided a significant (98%) reduction in the vertical RMS while utilising the corridor and grid images from the same flight height of 60 m.

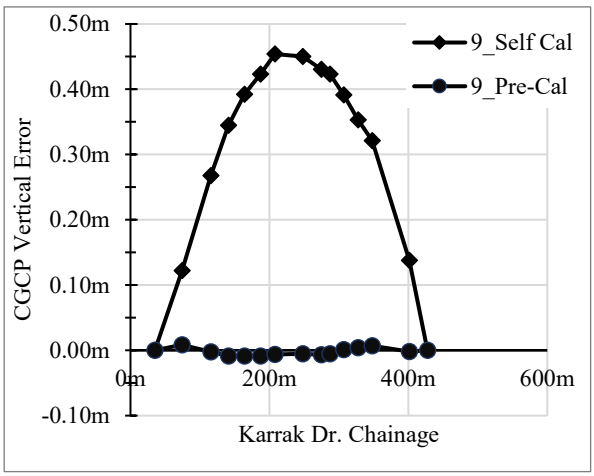

Figure 5: Comparison of image set 9; self-calibrated (squares) vs. pre-calibrated (circles) Vertical Error of CPs.

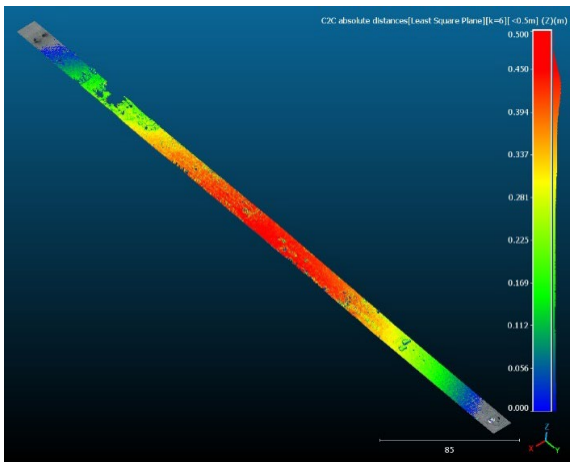

Figure 6. Comparison of Image Set 9; Self-Calibrated vs Pre-Calibrated Point Cloud Models.

Image sets 4 and 5 also used a combination of corridor and grid images. Set 4 utilised the images from the 60 m corridor and 80 m grid flights, while in set 5, the 80 m corridor and 60 m grid flight images were used. Interestingly both image sets using pre-calibration parameters provided a systematic height error of 0.038 m, with similar RMS and standard deviations. However, while the magnitude of the errors was similar, set 4 produced a -38 mm bow, while set 5 produced a +38 mm dome.

A comparison of image set 9 and set 5 in Figure 7 shows that set 5, with corridor and grid images at two flight heights, provided a significantly better self-calibrated model. The pre-calibrated model of set 9 of the corridor and grid images at the 60 m flight level returned more accurate results than set 5. Please note that set 9 self-calibration is shown in Figure 7 only partially, as the vertical errors are so huge. The complete shape or the set 9 self-calibration is shown in Figure 5. Figure 8 further illustrates the vertical differences between pre-calibrated point cloud models of sets 5 and 9.

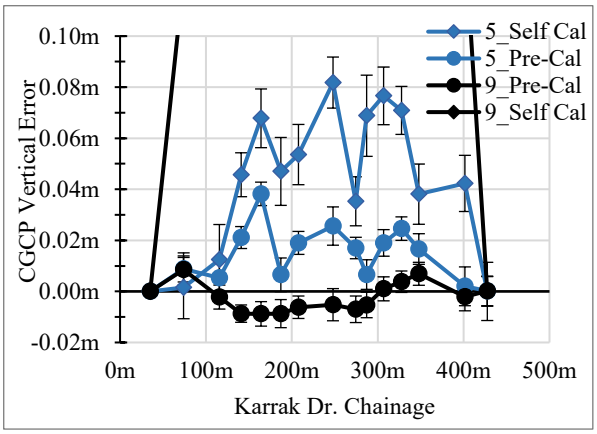

Figure 7. Comparison of Image Set 5 (Blue) and Set 9 (Black) CP Vertical Errors – Using self- (Square) and pre-(Circle) calibration.

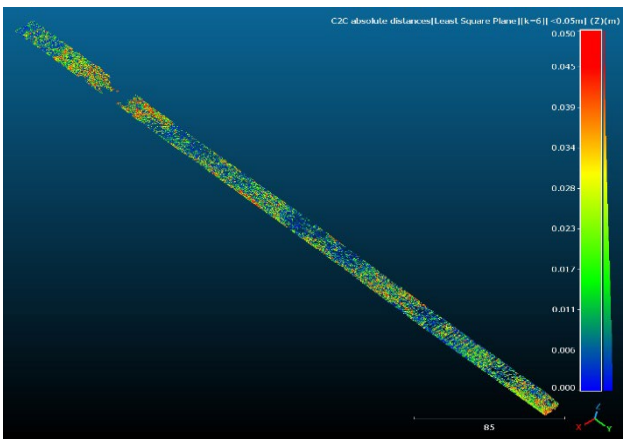

Figure 8. Comparison of Image Set 5 and Set 9; Pre-Calibrated Point Cloud Models.

As no correlation can be made for the self-calibrated image sets, the next step is to analyse the IOPs and assess the radial distortion corrections for correlation to the systematic error.

4.2 Camera Calibration

The calculated IOPs for each image set are shown in Table 4. The pre-calibration parameters from the car park PA2 were assumed to be 'true' and will be used as a reference for comparison. The focal lengths of these self-calibrated image sets have a standard deviation of 0.023 mm with a maximum residual of 0.07 mm.

Image Set	Pre-Cal	S_Cal Set 1	S_Cal Set 3	S_Cal Set 4	S_Cal Set 5	S_Cal Set 6	S_Cal Set 7	S_Cal Set 8	S_Cal Set 9	S_Cal Set 10	Std.Dev
C (mm)	8.622	8.640	8.632	8.697	8.650	8.631	8.633	8.607	8.658	8.639	0.023
PP x (mm)	0.041	0.055	0.036	0.050	0.041	0.036	0.040	0.037	0.039	0.035	0.007
PP y (mm)	0.010	0.032	0.009	0.066	0.027	0.005	0.021	-0.005	0.045	0.036	0.021

Table 4. Calculated interior Orientation Parameters for each self-calibrated image set.

Regarding the PA2 pre-calibration, it was found that a reduction in the number of GCP points to six, from 15, when performing a constrained camera calibration provided negligible differences in the calculated focal length (0.000%) and principal point offset in the X-axis (-0.005%).

In Figure 9, the radial distortion corrections (dr) for each set are plotted against the radial distance (r). The profile of the PA2 set, which is used as a reference, is shown in light blue. Sets 5, 8 and 7 have the lowest residuals compared to the reference, with residuals in the area above their distortion plots (Table 3) of +1.93 (-8.9%), -3.28 (15.2%) and -5.10 (28.9%), the vertical RMS of image sets 5, 8, and 7 are 0.051 m, 0.087 m, and 0.102 m, respectively, representing the lowest doming for all the self-calibrated sets. In comparison, sets 10, 1, and 4 have the highest level of doming (Table 3). These image sets showed a vertical RMS error of 0.606 m, 0.512 m, and 0.404 m, with their respective residuals of the distortion plot (Table 2) compared to the reference, which was -20.58 (95.4%), -34.78 (161.2%), and -39.7 (84.0%).

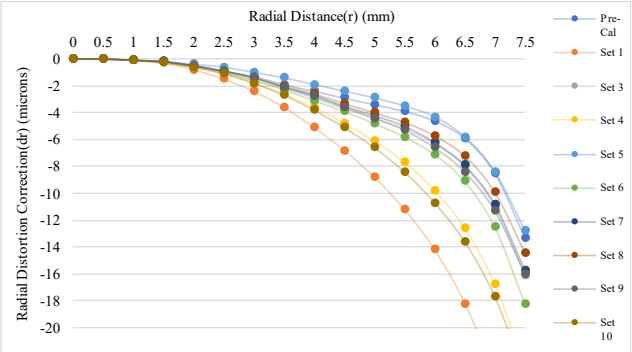

Figure 9. Radial Distortion Corrections (dr) in µm for on-the-job pre-calibrated image dataset vs self-calibrated image sets.

5. DISCUSSION AND CONCLUSION

This study supports the findings of multiple previous works; (James et al., 2017; James and Robson, 2014; Sanz-Ablanedo et al., 2020) concerning the existence of systematic dome-shaped errors that arise from inadequate camera calibration and incorrect radial distortion corrections. We analysed the benefit of investing in on-the-job pre-calibration to mitigate the doming prevalent in self-calibrating tests. In addition, an analysis of the impact of flight patterns on the vertical accuracy when surveying a road corridor. The test demonstrated the benefits of on-the-job pre-calibration overrides any benefits accrued from specific flight planning when performing self-calibration based on the corridor flights.

Analysis of the independent flight path combinations provided insights into the benefits of flight path selection to counter-doming under self-calibration flight. There is evidence that the introduction of POI flights in combination with corridor flights provided improvements to single grid or corridor flights. The self-calibrated corridor and POI flight combinations provided a lower average RMS of 0.150 m compared to the corridor and grid combinations of 0.350 m. This result agrees with the findings of (Sanz-Ablanedo et al., 2020) who suggested to use POI flights. However, the best result was returned by image set 5, consisting of an 80 m corridor and 60 m grid (0.051 m). This result could be considered as an anomaly. Nevertheless, we cannot substantiate that conclusion with the limited dataset available.

The hypothesis that performing a camera on-the-job pre-calibration can significantly reduce the elevation error on corridor surveys using UAV imagery compared to self-calibration programs, and the effect of flight paths and radial distortion correction on the self-calibration was demonstrated. Except for the single 60 m corridor from image set 1, all on-the-job pre-calibrated projects significantly outperformed those of the self-calibrated corridor flights. This indicates that systematic error can be reduced to acceptable levels using a simple flight design and on-the-job pre-calibration procedure using relatively simple imagery, negating the need for complex flight design, and extending flying times.

Whilst the self-calibrations continuously produced a doming error, irrespective of the selected flight paths, the results obtained when using the on-the-job pre-calibrated camera parameters included both doming and bowing errors, albeit significantly reduced compared to the self-calibrated results. As expected, analysing the impact of flight design on elevation errors confirms the risk of running a single flight path and the potential benefits of including a POI flight in the flight design.

On-the-job pre-calibrating the camera's IOPs requires additional fieldwork and processing hours. The time taken to undertake the on-the-job pre-calibration, estimated at 90 minutes in the field and 90 minutes for additional processing (hardware dependent), and is justified by the significant improvement of the results.

ACKNOWLEDGEMENTS

We want to acknowledge Trevor Carmichael for providing the UAV platform and offering his time to assist in data collection. We want to thank Prof. Clive Fraser for the access to iWintessPro. We also want to thank the reviewers for their valuable and constructive feedback which helped to improve the manuscript.

REFERENCES

Bojarczak, P., & Lesiak, P. (2021). UAVs in rail damage image diagnostics supported by deep-learning networks. Open Engineering, 11(1), 339–348.

Cledat, E., Cucci, D.A., Skaloud, J., 2020. Camera Calibration Models And Methods For Corridor Mapping with UAVS. ISPRS Annals of the Photogrammetry, Remote Sensing and Spatial Information Sciences, 2020, V-1-2020, pp.231-238.

CloudCompare. (2022). CloudCompare Version (V2.12.4). *CloudCompare 3D point cloud and mesh processing software Open-Source Project*. Retrieved from https://www.danielgm.net/cc/.

Cramer, M., Przybilla, H., & Zurhorst, A. (2017). UAV Cameras: Overview And Geometric Calibration Benchmark. *The International Archives Of The Photogrammetry, Remote Sensing And Spatial Information Sciences,* XLII-2/W6, 85-92.

Drone Deploy. (2023). Version (2.229.0). *drone deploy*. Retrieved from https://www.dronedeploy.com.

Eltner, A., & Schneider, D. (2015). Analysis of different methods for 3D reconstruction of natural surfaces from parallel-axes UAV images. *The Photogrammetric Record*, 30(151), 279–299. https://doi.org/10.1111/phor.12115

Fonstad, M., Dietrich, J., Courville, B., Jensen, J., & Carbonneau, P. (2013). Topographic structure from motion: a new development in photogrammetric measurement. *Earth Surface Processes and Landforms*, 38(4), 421-430.

Fraser, C. (1997). Digital camera self-calibration. I*SPRS Journal of Photogr. and Remote Sensing*, 52(4), 149-159.

Griffiths, D., & Burningham, H. (2018). Comparison of pre-and self-calibrated camera calibration models for UAS-derived nadir imagery for a SfM application. *Physical Geography: Earth And Environment*, 43(2), 215-235.

iWitness, 2019. https://www.photometrix.com.au/wp-content/uploads/2019/05/iWitnessPro-Camera-Calibration-Procedure-for-Drone-Imagery.pdf

James, M., & Robson, S. (2014). Mitigating systematic error in topographic models derived from UAV and ground-based image networks. *Earth Surface Processes and Landforms*, 39(10), 1413-1420.

James, M., Antoniazza, G., Robson, S., & Lane, S. (2020). Mitigating systematic error in topographic models for geomorphic change detection: accuracy, precision and considerations beyond off-nadir imagery. *Earth Surface Processes And Landforms*, 45(10), 2251-2271.

Ouédraogo, M. M., Degré, A., Debouche, C., & Lisein, J. (2014). The evaluation of Unmanned Aerial System-based photogrammetry and terrestrial laser scanning to generate Dems of agricultural watersheds. *Geomorphology*, 214, 339–355.

Park, S., & Choi, Y. (2020). Applications of unmanned aerial vehicles in mining from exploration to reclamation: A Review. *Minerals*, 10(8), 663.

Photometrix. (2018). iWitnessPRO^{TM} User Manual [PDF].

Photometrix. (2018). IWitnessProVersion (V4.104). Retrieved from https://www.photometrix.com.au/iwitnesspro-v4/.

Rupnik, E., Daakir, M., & Pierrot Deseilligny, M. (2017). MicMac – a free, open-source solution for photogrammetry. *Open Geospatial Data, Software and Standards*, 2(1).

Sanz-Ablanedo, E., Chandler, J., Ballesteros-Pérez, P., & Rodríguez-Pérez, J. (2020). Reducing systematic dome errors in digital elevation models through better UAV flight design. *Earth Surface Processes And Landforms*, 45(9), 2134-2147.

Turner, D., Lucieer, A., & Watson, C. (2012). An Automated Technique for Generating Georefrenced Mosaics from Ultra-High Resolution Unmanned Aerial Vehicle (UAV) Imagery, Based on Structure from Motion (SfM) Point Clouds. *Remote Sensing*, 4(5), 1392-1410.

Villanueva, J.K.S., Blanco, A.C., 2019. Optimization Of Ground Control Point (Gcp) Configuration For Unmanned Aerial Vehicle (UAV) Survey Using Structure From Motion (Sfm), The International Archives of the Photogrammetry, Remote Sensing and Spatial Information Sciences, Volume XLII 4/W12, pp. 167 174, 2019.

Williams, K. (2005). Digital Vertical Aerial Camera System for High-Resolution Site Inspections in Conservation Easement Monitoring. *Electronic Thesis and Dissertations*, 438.